Physics of blastocoel formation by hydro-osmotic lumen coarsening

Mathieu Le Verge–Serandour[1] and Hervé Turlier[1,2]

[1]Center for Interdisciplinary Research in Biology, Collège de France, PSL Research University, CNRS UMR7241, INSERM U1050, 75005 Paris, France.

The blastocoel is a fluid-filled cavity characterizing early embryos at blastula stage. It is commonly described as the result of cell division patterning, but in tightly compacted embryos the mechanism underlying its emergence remains unclear. Based on experimental observations, we discuss an alternative physical model by which a single cavity forms by growth and coarsening of myriad of micrometric lumens interconnected through the intercellular space. Considering explicitly ion and fluid exchanges, we find that cavity formation is primarily controlled by hydraulic fluxes, with a minor influence of osmotic heterogeneities on the dynamics. Performing extensive numerical simulations on 1-dimensional chains of lumens, we show that coarsening is self-similar with a dynamic scaling exponent reminiscent of dewetting films over a large range of ion and water permeability values. Adding active pumping of ions to account for lumen growth largely enriches the dynamics: it prevents from collective collapse and leads to the emergence of a novel coalescence-dominated regime exhibiting a distinct scaling law. Finally, we prove that a spatial bias in pumping may be sufficient to position the final cavity, delineating hence a novel mode of symmetry breaking for tissue patterning. Providing generic testable predictions our hydro-osmotic coarsening theory highlights the essential roles of hydraulic and osmotic flows in development, with expected applications in early embryogenesis and lumenogenesis.

Embryogenesis | Lumen | Coarsening | Osmotic effect | Symmetry breaking

[2] **Correspondence:** *herve.turlier@college-de-france.fr*

The blastula is the first identifiable stage of early embryo development that is common to most animals, and consists most generally in a hollow epithelial layer enclosing a fluid-filled cavity - the blastocoel. Blastocoel emergence is classically described as the outcome of cell cleavage patterning, where successive divisions take place along the surface plane of the embryo to direct the organization of blastomeres in a spherical sheet (1). Planar divisions appear indeed sufficient to explain the formation of a blastocoelic cavity in several early invertebrate embryos, such as cnidarians or echinoderms (2, 3), as supported by numerical simulations (4, 5). In this scenario, the first cleavages leave an initial intercellular space between loosely adhering blastomeres, that is then amplified in volume by consecutive planary-oriented divisions. Such mechanism requires water to be able to freely move through the nascent epithelial layer to fill the central cavity, but in various vertebrate embryos such as mammals (eutherians) (6), and, to a certain extent, amphibian embryos (7), the epithelial layer may be already sealed by tight junctions before blastocoel formation. How a cavity might emerge in tightly packed and sealed morulae from division patterning alone remains unclear.

Recently, we uncovered a possible alternative mechanism in mouse embryos (8), whereby adhesive contacts are hydraulically fractured into myriad of microcavities (also called microlumens) that progressively coarsen into a single cavity, most likely through fluid exchange within the ∼ 50nm wide intercellular space (9, 10) (Fig. 1). In fact, similar micronsized fluid-filled compartements had been already observed at the cell-cell contacts of various embryos preceding blastocoel formation: in mammals (11, 12), in amphibians (13–15) and even in *C.elegans*, although for the latter the resulting cavity rapidly disappears (16). Such transient coarsening phase may have been missed in other species having a tightly compacted morula prior to blastula stage, because of the need to image section planes of the embryo with a high spatiotemporal resolution in order to identify microlumens. In this alternatative mechanism, the fluid that will fill the final cavity cannot directly pass a sealed epithelial barrier, and has to be pumped by an osmotic gradient from the external medium into the intercellular space, hightlighting an evident coupling between hydraulic and osmotic effects. The requirement of ion pumping has, in fact, already been well documented in mammalian embryos (17–21), and some evidence of osmotic control of blastocoel formation in other embryo types was already put forward earlier (22–24). Yet, little is known about the hydro-osmotic control of blastocoel formation from a physics perspective. In vitro, MDCK monolayers spontaneously generate fluid-filled domes (also called blisters) as well when they are plated on a 2D glass surface (25, 26), and cysts in 3D when they are maintained in suspension (27, 28). This process is characterized by active ion pumping toward the basal side of cells, triggering water uptake in the apico-basal direction. It is indeed important to remark that blastocoel-like cavities emerge at the baso-lateral side of polarized cells, that is typically adhesive. They differ hence topologically from apical lumens, that are facing apical -and intrinsically non-adherent- cell interfaces (29, 30). Apical lumens are directly sealed at their surface by tight junction proteins (31), limiting paracellular water leaking into the intercellular space, while allowing for the passage of selected ions (32). Such important topological differences may explain why baso-lateral cavities, in contrast to their apical counterparts, appear systematically pressurized, as they need to grow against adhesive contacts; it may also explain why tissues with multiple apical lumens may fail to spontaneously resolve into a single cavity (33).

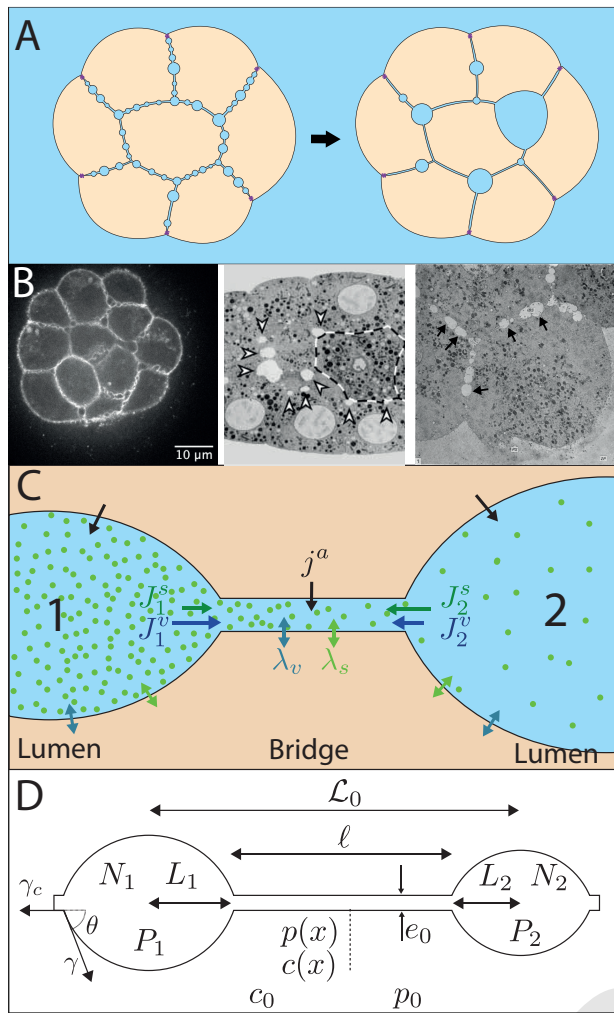Hydraulic and osmotic flows are more and more recog-

Fig. 1. (A) Schematic of the coarsening process to explain the formation of a single blastocoel cavity from a network of microlumens. (B) Examples of microlumen networks in various early embryos. Left: fluorescence microscopy confocal section of a mouse embryo at 32-cell stage (8). Center: Electron micrograph of a 28-cell *C.elegans* embryo (16). Right: Electron micrograph of a 9-cell rhesus monkey embryo (12). (C) Lumens are modeled as distinct compartments interconnected through an intercellular bridge. They can exchange water (v) and solutes (s) with each others through the bridge (fluxes J_i^v and J_i^s) and with surrounding cells by active pumping of rate j^a and through passive permeation of coefficients λ_v, λ_s. (D) Parametrization of the two-lumen system: each lumen is characterized by its length $L_i = (\mu A_i)^{1/2}$, concentration C_i and pressure P_i; the intercellular bridge is characterized by its length $\ell(t)$, thickness e_0, and position-dependent solute concentration $c(x)$ and hydrostatic pressure $p(x)$.

nized as essential determinants of embryo and tissue shaping (8, 32, 34–38). However only a few physical models describe the interplay between cell mechanics, osmotic effects and fluid flow in morphogenesis (39–42) and in previous models, osmolarity is most generally considered spatially homogeneous. Here, we propose a generic hydro-osmotic physical model for the formation of a cavity that explicitly accounts for ion pumping and osmotic gradients (Fig. 1C). We do not study, however, the prior nucleation process of microcavities, which likely involves a hydraulic fracturing of cell-cell contacts (43). We start on the contrary from a preformed and contiguous network of microlumens (Figs. 1A-B) and we focus on their collective dynamics using numerical simulations and mean-field theory. For the sake of simplicity, we also

neglect ion charges and membrane potentials and consider a single solute only, following similar hypotheses as a recent model for a single apical lumen (34).

Coupled dynamics for two lumens

In this first section, we focus on a two lumens system to introduce the fundamental dynamic equations and to characterize the competition between hydraulic and osmotic effects.

Dynamical equations. Dynamical equations for two lumens are derived from conservation equations of mass and solutes. The lumens are represented as 2-dimensional compartments connected through a 1-dimensional bridge of width e_0 and length ℓ along the x-direction (Fig. 1D). Each lumen $i = 1, 2$ is described by its area A_i, its hydrostatic pressure P_i and its concentration $C_i = \frac{N_i}{A_i}$, supposed homogeneous, where N_i is the number of solutes (in moles). A lumen is pressurized by a tension γ supposed constant, leading to a Laplace's pressure jump $\delta P_i = P_i - p_0 = \gamma \sin\theta / \sqrt{\mu A_i}$ across the membrane, where μ is a constant that depends on the contact angle $\theta = \arccos \gamma_c / \gamma$ between the lumens and the bridge with γ_c the adhesive tension in the bridge (see SI text and Fig. 1D). The lumens and the bridge are delimited by two lateral membranes of water and solutes permeability coefficients λ_v and λ_s respectively and are embedded in a an infinite "cellular" medium acting as a chemostat of concentration c_0 and as a barostat of pressure p_0 (Fig. 1C). The mass in a lumen i is modified through a longitudinal hydraulic flux J_i^v toward the bridge and through lateral osmotic fluxes from the cellular medium, that stem from the imbalance between osmotic and hydraulic pressure across membranes. We rewrite mass balance as function of the lumen length $L_i = \sqrt{\mu A_i}$

$$\frac{dL_i}{dt} = 2\mu\nu\lambda_v \big[\mathcal{R}T\delta C_i - \delta P_i \big] - \frac{\mu}{2L_i} J_i^v, \qquad (1)$$

where $\mathcal{R}$ is the gas constant, T the temperature, $\delta C_i = C_i - c_0$ is the concentration jump across the membranes, and ν is a geometrical constant function of θ (see SI text). The hydraulic flux J_i^v is calculated from boundary conditions in the bridge. The number of moles of solutes in each lumen N_i similarly varies through an outgoing flux J_i^s toward the bridge and through lateral passive fluxes, triggered by the chemical potential difference of the solute across membranes. Adding an active pumping rate j^a by unit membrane length, solute balance reads

$$\frac{dN_i}{dt} = 2\nu L_i \left[\lambda_s \mathcal{R}T \log\left(\frac{c_0}{C_j} \right) + j^a \right] - J_i^s \qquad (2)$$

Conservation equations in the bridge are written along its length $\ell(t)$ in the x-direction. Local mass balance is obtained by calculating incoming and outgoing longitudinal fluxes along the x-axis and lateral osmotic fluxes across the membranes. The longitudinal flux is given by the 2D Poiseuille's flow $q(x) = -\kappa_v \frac{\partial \delta p}{\partial x}$, where $\kappa_v \approx \frac{e_0^3}{12\eta}$ is the hydraulic conductivity, inversely proportional to the solvent viscosity η.

Considering a passive lateral flux of solvent along the two membrane sides, like for the lumens, yields

$$\kappa_v \frac{\partial^2 \delta p}{\partial x^2} + 2\lambda_v \left[\mathcal{R}T\delta c(x) - \delta p(x) \right] = 0 \qquad (3)$$

where $\delta c(x) = c(x) - c_0$ and $\delta p(x) = p(x) - p_0$ are local concentration and pressure jumps across the membrane. The balance of solutes along the bridge is similarly given by the sum of a longitudinal diffusive flux $e_0 j_d(x) = -e_0 D \frac{\partial \delta c}{\partial x}$ (Fick's law with diffusion coefficient D) and passive lateral fluxes of solutes across the two membrane sides, driven by the imbalance of chemical potential for the solute. Adding an active pumping rate of solutes j^a yields

$$e_0 D \frac{\partial^2 \delta c}{\partial x^2} = 2\mathcal{R}T\lambda_s \log\left(1 + \frac{\delta c}{c_0}\right) - 2j^a \qquad (4)$$

where we assumed that the relaxation of concentration in the bridge is very fast compared to other timescales in the problem $\frac{\partial c}{\partial t} \sim 0$ (see SI text). Similarly to (34), solvent and solute exchange along the bridge are found to be controlled by two characteristic length scales

$$\xi_v = \sqrt{\frac{\kappa_v}{2\lambda_v}}, \qquad \xi_s = \sqrt{\frac{De_0 c_0}{2\lambda_s \mathcal{R}T}} \qquad (5)$$

which measure the relative magnitude of longitudinal and lateral passive fluxes of solvent (v) and solutes (s) respectively. They play the roles of screening lengths: a pressure (resp. concentration) gradient along the bridge will be screened on a length larger than ξ_v (resp. ξ_s). Therefore, for $\ell \gg \xi_v$ (resp. $\ell \gg \xi_s$), we expect the lumens to become hydraulically (resp. osmotically) uncoupled . On the contrary, for $\ell \ll \xi_{v,s}$, pressure or concentration differences along the bridge may trigger solvent or solute fluxes from one lumen to the other. In the rest of the manuscript, we will denote by screening lengths the dimensionless ratios $\chi_{s,v} \equiv \xi_{s,v}/\ell_0$, where absolute screening lengths $\xi_{s,v}$ have been rescaled by the mean initial bridge length $\ell_0 = \langle \ell(0) \rangle$. We use these ratios as global parameters to characterize screening effects in our system, but it should be noted that the actual pressure or concentration screening varies in fact in time with the length of the bridge $\ell(t)$. Interestingly, we observed that the ratio $\xi_{v,s}/\ell(t)$ measures roughly the average number of neighbors one lumen can "see" from a hydraulic or osmotic perspective.

To simplify our equations, we remark that the typical hydrostatic pressure jump across the plasma membrane of embryonic cells $\delta P_i \sim \delta p \sim 10^{2-3}$ Pa is a few orders of magnitude lower than the absolute value of osmotic pressure $\Pi_0 = \mathcal{R}Tc_0 \sim 10^5$ Pa. This implies that $\delta C_i, \delta c \ll c_0$ (see SI text) and allows us to derive analytic solutions for solvent and solute fluxes $\pm q(x)$ and $\pm e_0 j_d(x)$ from the bridge equations Eq. (3) and Eq. (4). By equating these fluxes, evaluated at bridge boundaries $x = \mp \ell(t)/2$ with outgoing fluxes from the lumens J_i^v, J_i^s for $i = 1, 2$, and by fixing the system size $\mathcal{L}_0 = L_1(t) + L_2(t) + \ell(t) = $ cte, we close our system of equations (see SI text). Denoting L_0 and N_0 the mean initial lumen size and solute number, we introduce the following dimensionless variables $L_i = \bar{L}_i L_0$, $\ell = \bar{\ell}\ell_0$, $N_i = \bar{N}_i N_0$,
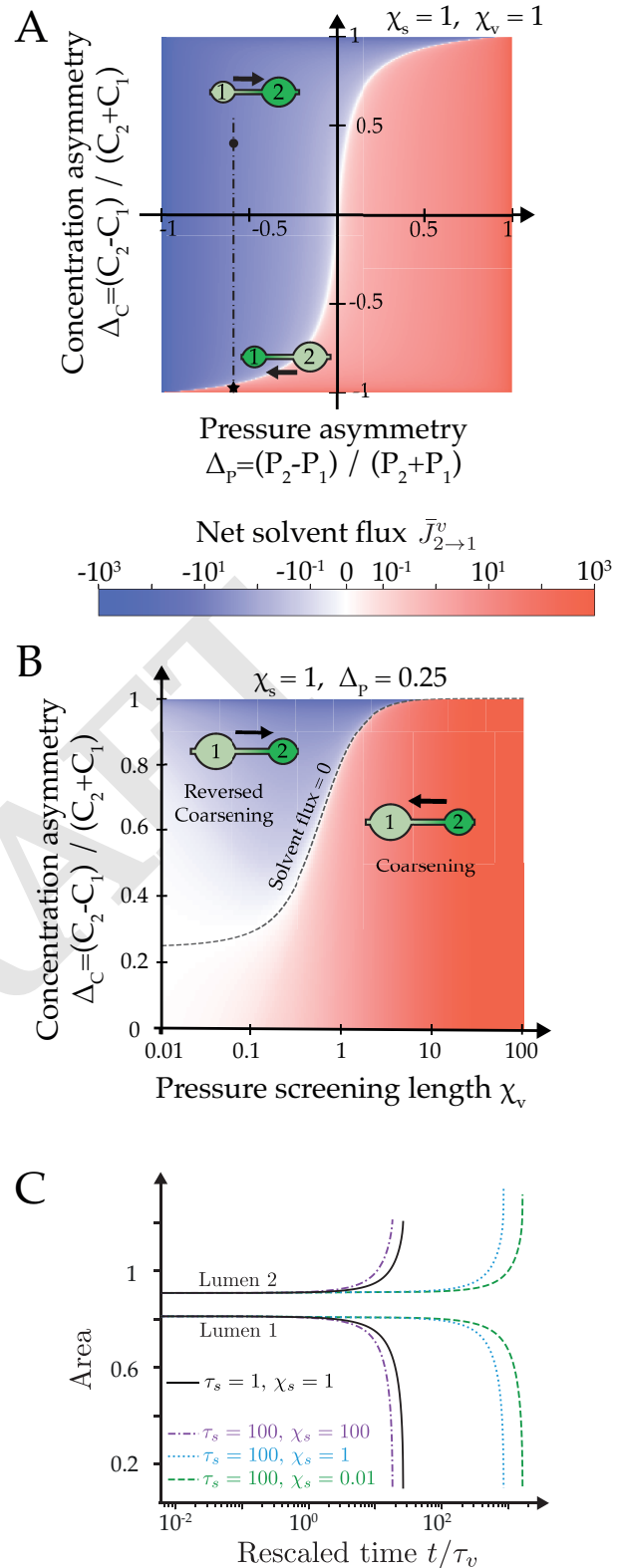

Fig. 2. (A) Diagram of the net flow $\bar{J}_{2\to1}^v = \bar{J}_2^v - \bar{J}_1^v$ as a function of concentration and pressure asymmetries Δ_C and Δ_P, for $\chi_{s,v} = 1$. The flow direction is schematized for two sets of values (Δ_P, Δ_C). (B) Diagram of the net flow $\bar{J}_{2\to1}^v$ as function of the concentration asymmetry Δ_C and pressure screening lengths χ_v for $\chi_s = 1$ and $\Delta_P = 0.25$. (C) Time evolution of the area of two lumens as function of χ_s and τ_s. Other simulation parameters are $\chi_v = 10$, $\tau_v = 1$ s.

$j^a = \bar{j}^a \lambda_s \mathcal{R}T$, $J_i^v = \bar{J}_i^v \frac{L_0^2}{\tau_v}$, $\bar{J}_i^s = \bar{J}_i^s \frac{N_0}{\tau_s}$, and dimensionless parameters $N_0 = c_0 L_0^2$ and $\epsilon = \frac{\gamma \sin\theta}{L_0 \Pi_0}$. The dynamics of the system reduces finally to four coupled ordinary differential equations (ODEs) for $\bar{N}_i$ and $\bar{L}_i$ ($i = 1, 2$):

$$\tau_v \frac{d\bar{L}_i}{dt} = \mu\nu \left[\mu \frac{\bar{N}_i}{\bar{L}_i^2} - 1 - \frac{\epsilon}{\bar{L}_i} \right] - \frac{\mu}{2\bar{L}_i} \bar{J}_i^v \quad \textbf{(6)}$$

$$\tau_s \frac{d\bar{N}_i}{dt} = 2\nu \bar{L}_i \left[1 - \mu \frac{\bar{N}_i}{\bar{L}_i^2} + \bar{j}^a \right] - \bar{J}_i^s \quad \textbf{(7)}$$

$$1 = 2\bar{L}_1 + 2\bar{L}_2 + \bar{\ell} \quad \textbf{(8)}$$

where outgoing fluxes $\bar{J}_i^{v,s} = f_i^{v,s}(\bar{N}_{1,2}, \bar{L}_{1,2}, \bar{\ell})$ are functions coupling dynamically the two lumens $i = 1, 2$. The dynamics is controlled by the following solvent and solute equilibration timescales

$$\tau_v = \frac{L_0}{2\lambda_v \Pi_0}, \qquad \tau_s = \frac{L_0 c_0}{2\lambda_s \mathcal{R}T} \quad \textbf{(9)}$$

Hydro-osmotic control of coarsening. To characterize the competition between osmotic and hydraulic effects, we focus first on the factors controlling the instantaneous net solvent flow between two lumens. Any asymmetry in size or tension between two lumens is expected to generate a hydrostatic pressure difference $\delta\bar{P}$, triggering a net solvent flow $\bar{J}_{2\to1}^v = \bar{J}_2^v - \bar{J}_1^v$. But the bridge may also act as an (imperfect) semi-permeable membrane, that can carry osmotically-driven solvent flows if a concentration difference $\delta\bar{C}$ exists between the lumens. These two kinds of solvent flows, hydraulic and osmotic, may enter in competition if $\delta\bar{C}\delta\bar{P} > 0$, as shown in Fig. 2A where we plotted the signed value of the net flow $\bar{J}_{2\to1}^v$ as function of concentration and pressure asymmetries $\Delta_C = (C_2 - C_1)/(C_2 + C_1)$ and $\Delta_P = (P_2 - P_1)/(P_2 + P_1)$. For a given set of screening lengths $\chi_v, \chi_s \sim 1$, the net solvent flow direction expected from Laplace's pressure (from small to large lumens) may be outcompeted by an osmotic flow in the reverse direction if a sufficiently large concentration asymmetry exists between the two lumens. In practice, we observe that the relative asymmetry has to be much larger for concentrations than for pressures to reverse the coarsening direction. This let us anticipate already a limited influence of osmotic gradients, in general, on lumen dynamics. As a further indication for this trend, we find that the magnitude of the solvent flow depends primarily on the pressure screening length χ_v (Fig. 2B), while the screening of concentration asymmetries has no measurable effect for $\chi_s > 1$ and only a mild influence for $\chi_s < 1$ (see Fig. S1). From a dynamical point of view, osmotic effects could however have a strong influence in the limit $\tau_s \gg \tau_v$ and $\chi_s \ll 1$, where solutes are expected to become almost trapped in lumens, their exchange dynamics with the cellular medium and other lumens being largely slowed down. Indeed, if the size of a given lumen drops rapidly, its solute concentration will rise (see Fig. S2B), generating an osmotically-driven solvent flow that may oppose to the pressure-driven flow. This effect, reminiscent of the osmotic stabilization of emulsions and foams by trapped species (45, 46), is illustrated in Fig.2C where we

plot the dynamics of two lumens starting at osmotic equilibrium for $\tau_s = 100\tau_v$ and for decreasing values of χ_s from 100 to 10^{-2} ($\chi_v = 10$). In this regime, we observe that the coarsening dynamics is slowed down by a few orders of magnitude through the combined effects of slow solute relaxation and large concentration screening. However, and in contrary to foams or emulsions (45, 46), our system cannot reach complete stabilization, since lumens ultimately homogenize their concentrations by exchanging fluid with surrounding cells.
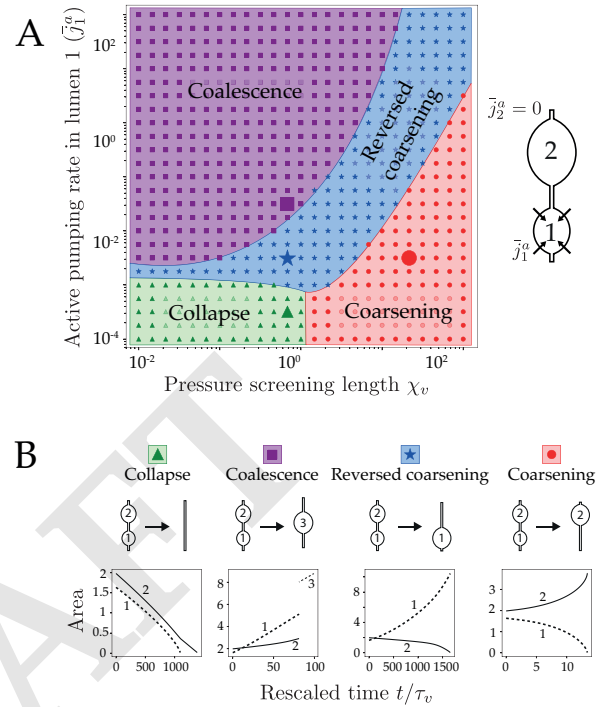

Fig. 3. (A) Fate diagram for 2 lumens as function of the active pumping $\bar{j}_1^a$ of lumen 1 and pressure screening length χ_v, at fixed $\chi_s = 1$. Four behaviors are found numerically: collapse for large screening and low pumping, coarsening and reversed coarsening at intermediate values and coalescence for large pumping. The delineation of the regions have been drawn by hand, for presentation purpose. (B) Typical time evolution of the areas of lumen 1 (dotted line) and lumen 2 (full line) in the four cases.

Influence of active pumping. Then, we explore the influence of active pumping on the dynamics of two lumens. Ion pumps, such as the Na/K ATPase, can actively transport ions from/to the cell against the chemical potential difference across the membrane by hydrolyzing ATP. Here, we consider an initial size ratio $L_2(0)/L_1(0) = 1.1$ and a nonzero pumping rate $\bar{j}_1^a$ in the lumen 1 only ($\bar{j}_2^a = 0$). We plot in Fig. 3 the outcome (or fate) of the two lumens as function of $\bar{j}_1^a$ and χ_v. We identify four different possible fates: collapse of the two lumens (triangles), coarsening $1 \to 2$ (disks), reversed coarsening $2 \to 1$ (stars) and coalescence (squares). At vanishing pumping $\bar{j}_1^a \sim 0$, both lumens are under tension and may either coarsen if their pressure difference is not screened ($\chi_v \gtrsim 1$) or collapse at large pressure screening ($\chi_v \lesssim 1$). When pumping is increased in the lumen 1, a third regime that we called reversed coarsening appears, where the coarsening direction is inverse to the one expected from the initial size asymmetry: this happens when the pumping-driven growth of the lumen 1 overcomes its discharge into the lumen

Le Verge–Serandour *et al.* | Hydro-osmotic lumen coarsening

2, reversing the flow direction. Above some pumping rate a fourth dynamical regime appears, where growth is faster than hydraulic coarsening leading to lumen collision and coalescence. We find therefore that active pumping can greatly modify the dynamics of two lumens, which let us anticipate its major role in the coarsening of a network of lumens.

Coarsening dynamics for a 1-dimensional chain

In this section, we turn to the dynamics of a 1-dimensional chain of $\mathcal{N}$ lumens (Fig. 4A). Each lumen of label i is described by its position, its size $L_i = \sqrt{\mu A_i}$ and its number of moles of solutes N_i, and is connected to up to two neighboring lumens by a bridge (i,j) of length $\ell_{ij}(t)$. The chain has a fixed total length $\mathcal{L}_0 = 2\sum_i L_i(t) + \sum_{\{ij\}} \ell_{ij}(t)$ and its borders are fixed and sealed. We generate initial chain configurations by chosing lumens areas A_i and bridges lengths ℓ_{ij} from Gaussian distributions of respective means $A_0 = 1$ and $\ell_0 = 10$, and respective standard deviations 0.2 and 2. All our simulations start at osmotic equilibrium ($\delta C_i = \delta c = 0$), and unless otherwise specified we set $\tau_v = \tau_s = 1s$ The coupled ODEs Eq. (6) Eq. (7) for the lumens $i = 1, N$ are integrated numerically leading to the typical lumen dynamics shown in Fig. 4A. After a few steps, some lumens may collapse or enter in collision; when such topological events happen, the integration is stopped, the configuration of the chain is recalculated to remove or merge implicated lumens before restarting the integration (see Materials & Methods and SI text).

Coarsening without pumping. To charaterize the average dynamics of a chain, we plot in Fig. 4B the number of lumens as function of time for various values of the initial screening lengths χ_v and χ_s. After a plateau, we generically observe a coarsening behavior characterized by a dynamic scaling law $\mathcal{N}(t) \propto t^{-\frac{2}{5}}$. This scaling exponent is in fact reminiscent of the dynamics of a purely hydraulic chain of droplets (47–49). In the limit of small χ_v, we observe yet a rapid collapse of the chain, indicative of the overall uncoupling of lumens. As far as the lumens remain hydraulically coupled to their nearest neighbor, the scaling exponent remains unaffected by the amplitude of solvent and solute screenings (Fig. 4B). The main difference with a pure hydraulic dynamics can be observed in the onset of coarsening, that is characterized by a typical timescale $T_h = \frac{2\tau_v \ell_0 L_0}{\mu \epsilon \xi_v^2} = \frac{2\ell_0 L_0^3}{\mu \sin\theta \gamma \kappa_v}$ that increases with a decreasing pressure screening length ξ_v. To understand the link between our dynamics and a pure hydraulic system, we consider the limit $\chi_v \gg 1$, $\chi_s \ll 1$, and $\tau_s \ll \tau_v$, where concentrations relax rapidly and lumens are fully coupled hydraulically. In this limit, our system of equations reduces to a single dynamical equation where the contribution of solutes has vanished and that reveals analytically equivalent to the one proposed in (50, 51) to describe coarsening in dewetting films (see SI):

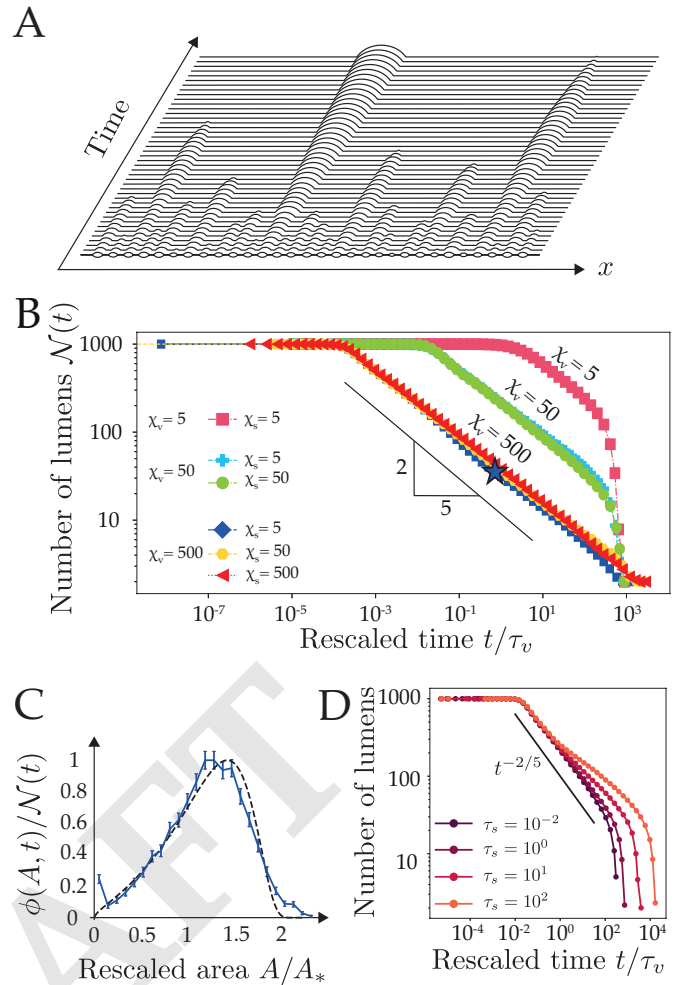$$\frac{dL_i}{dt} = \frac{1}{T_h \ell_{ij} L_i}\left(\frac{1}{L_j} - \frac{1}{L_i}\right) \qquad (10)$$

Fig. 4. (A) Typical spatiotemporal hydro-osmotic coarsening dynamics of a 1-dimensional chain. Here $\mathcal{N}(0) = 30$ lumens evolve from osmotic equilibrium with $\chi_v = 100$, $\chi_s = 1$, $\tau_{s,v} = 1\,s$. (B) Plot of the number of lumens as function of the rescaled time t/τ_v for various values of the screening lengths $\chi_{v,s}$ where each simulation starts at $\mathcal{N}(0) = 1000$ lumens. Each curve is an average of 20 simulations. The scaling law $t^{-2/5}$ (black line) is shown as a guide for the eye. (C) Lumen area distribution as function of rescaled area A/A_*, where $A_* = \int A\phi(A,t)dA$ is the mean field area with respect to this distribution. The plain curve is an average over 100 simulations with $\chi_v = 500$, $\chi_s = 5$ and taken at the time-point indicated by a star on panel B. The dashed line is the theoretical self-similar distribution given in the SI. (D) Plot of the number of lumens as function of the rescaled time t/τ_v for $\tau_v = 1\,s$, $\chi_v = 50$, $\chi_s = 5$ and increasing values of the solute relaxation time τ_s from $10^{-2}\,s$ to $10^2\,s$. A deviation from the scaling law $t^{-2/5}$ (plotted in plain line as a reference) is observed for large τ_s, indicative of an osmotic stabilization effect, which slows down the coarsening.

We will refer to this limit as the *hydraulic chain*, where osmotic effects have disappeared. In such limit, the scaling law for the number of lumens $\mathcal{N}(t) \sim t^{-2/5}$ as well as the distribution of lumens size $\phi(A,t)$ can be predicted from a mean-field theory of Lifshitz-Slyosov-Wagner type (see SI text) (50–52). In Fig. 4C, we compare the size distributions of lumens predicted by the hydraulic chain mean field theory and obtained from our simulations for $\chi_v = 500$, $\chi_s = 5$. The very close agreement indicates that the hydraulic chain limit is generically a good approximation for the behavior of a hydro-osmotic chain. To challenge the validity of the hydraulic chain approximation, we chose parameters favoring the retention of solutes in lumens, as for the two-lumen sys-

tem (Fig. 2C). In Fig. 4D we plot the time evolution of the chain for increasingly slower solute equilibration (increasing τ_s) and we find indeed a deviation from the scaling law $t^{-2/5}$ when $\tau_s \gg 1$, indicative of a slowing-down of coarsening. Like for the two-lumen system, solutes are transiently trapped within lumens, which triggers larger osmotic asymmetries between lumens that may compete with pressure-difference driven flows and slow down the hydraulic coarsening of the chain (Fig. S2C).
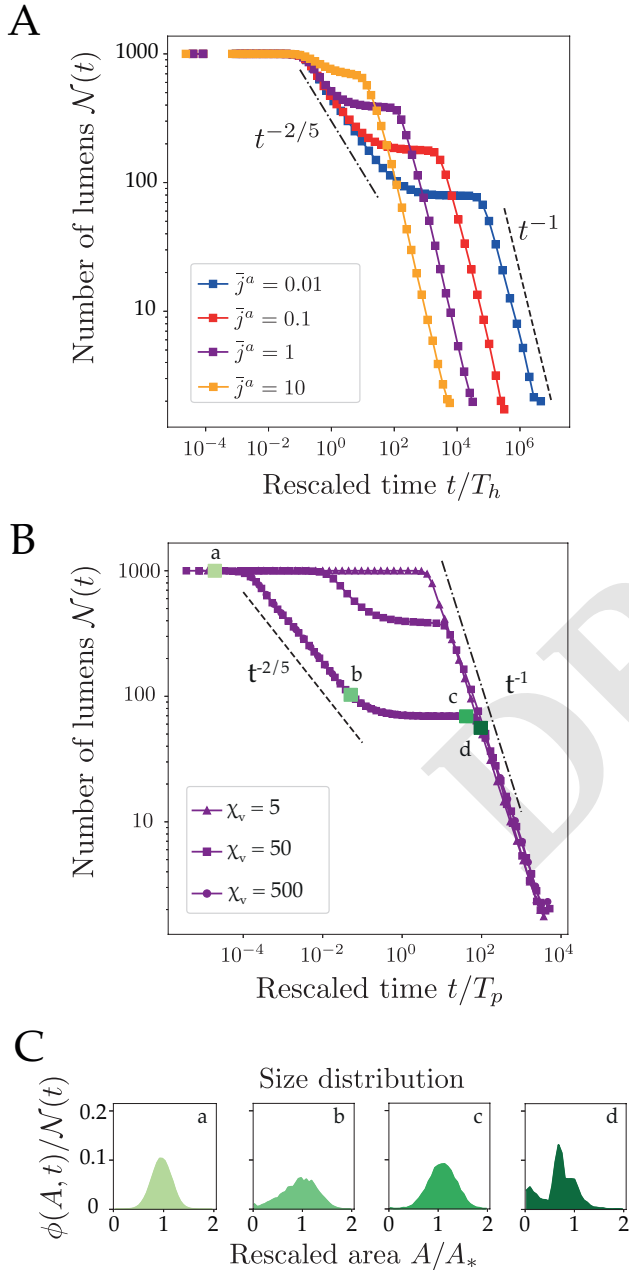

Fig. 5. (A) Coarsening of 1-dimensional chains with uniform active pumping j^a: plot of the number of lumens as function of the rescaled time t/T_h for increasing values of the pumping rate $\bar{j}^a = 10^{-2}, 10^{-1}, 1$ and 10. Each curve is the average over 20 simulations with screening lengths $\chi_v = 50, \chi_s = 5$. (B) Number of lumens as function of the rescaled time t/T_p for three values of the pressure screening length χ_v, for $\bar{j}^a = 1$ and $\chi_s = 5$. (C) Area distribution $\phi(A, t)$ at four different times indicated on the plot in (B), with 100 simulations.

Coarsening with active pumping. We finally study the influence of active pumping of solutes on the chain dynamics. We first assume a homogeneous pumping rate $\bar{j}^a$ along the chain. In Fig. 5A we plot the time evolution of the number of lumens $\mathcal{N}$ as function of t/T_h for increasing values of the pumping rate $\bar{j}^a$ from 10^{-2} to 10 ($\chi_{v,s} = 50$). The dynamics is now typically characterized by two coarsening phases that are separated by a novel timescale $T_p = \frac{\tau_v}{\mu\nu\,j^a} = \frac{\lambda_s L_0 \mathcal{R}T}{2\lambda_v \Pi_0\,j^a}$. This timescale measures the competition between active solute pumping, controlled by j^a, and passive solute relaxation, controlled by λ_s, in triggering solvent permeation, limited by λ_v. For $t \ll T_p$ we recover the hydraulic chain limit characterized by a power-law $t^{-2/5}$ as previously. For $t \gg T_p$, the number of lumens first stabilizes into a plateau before decreasing again with a novel scaling law $\mathcal{N}(t) \sim t^{-1}$. This novel coarsening regime is dominated by lumen coalescence and may be understood with the following arguments. Considering the previous hydraulic chain limit ($\chi_v \gg 1, \chi_s \ll 1$ and $\tau_s \ll \tau_v$) with nonzero $\bar{j}^a$, we can derive a modified expression for lumen dynamics (see SI text)

$$\frac{dL_i}{dt} = \frac{1}{T_h \ell_{ij} L_i}\left[\frac{1}{L_j} - \frac{1}{L_i}\right] + \frac{1}{T_p} \tag{11}$$

In this limit, the last term in Eq. (11) is inversely proportional to T_p and corresponds exactly to the rate of osmotic lumen growth triggered by active pumping. Taking the limit $t \gg T_p$ Eq. (11) becomes $\frac{dL_i}{dt} \simeq \frac{1}{T_p}$, and using length conservation $\bar{L}_{ij} = \bar{L}_i(t) + \bar{L}_j(t) + \bar{\ell}_{ij}(t)$, it yields $\frac{d\ell_{ij}}{dt} \simeq -\frac{2}{T_p}$. The average length of bridges decreases therefore linearly in time, such that the rate of coalescence will naturally scale as $\mathcal{N}(t) \sim (t/T_p)^{-1}$, as shown on Figs. 5A and B. For large enough pumping rate $\bar{j}^a$, we reach a limit where $T_p \sim T_h$, such that the hydraulic coarsening phase disappears, leaving only a coalescence-dominated coarsening dynamics, as we observe on Figs. 5A and B. On Fig. 5C we plot the size distribution of lumens at various time-points of a dynamics where hydraulic and coalescence dominated regimes are well separated in time ($\bar{j}^a = 1$). Starting from the Gaussian used to generate the chain, the distribution first evolves toward the asymmetric long-tailed distribution characteristic of hydraulic coarsening (Fig. 4C). The transition toward the coalescence phase is characterized by a plateau for the number of lumen and a peaked distribution of lumen sizes, indicative of a collective growth phase with size homogenization of the lumens. This size homogenization can be understood by the fact that lumens become hydraulically uncoupled while coalescence has not yet started, leading to a narrowing of the distribution (see SI text). The coalescence-dominated regime exhibits then a multimodal distribution, that reveals subpopulations of lumens forming by successive waves of coalescence.

Finally, we study how heterogeneities in active pumping within an embryo may bias the position of the final blastocoel. In mammalian embryos, the formation of the blastocoel relies on transepithelial active transport of ions and water from the external medium to the intercellular space by an apico-basally polarized cell layer, the trophectoderm

(TE) (20, 53). We expect therefore that active pumping may be essentially concentrated at cell interfaces with outer cells (TE), rather than at the ones between inner cells (called ICM for inner cell mass) as illustrated on Fig. 6A. To study the effect of a spatial bias in active pumping, we consider a chain of $\mathcal{N}(0) = 100$ lumens and $\chi_v = 500$, and we perturb an uniform pumping profile with a Gaussian function $\bar{j}^a(x) = \bar{j}^a_0 + \frac{\delta \bar{j}^a}{\sqrt{2\pi}\sigma} \exp\left(\frac{(x-\mu)^2}{\sigma^2}\right)$ that is shifted from the chain center ($\mu = 0.4$, $\sigma = 0.05$). We simulate the chain dynamics keeping the amplitude $\delta \bar{j}^a = 1$ of the Gaussian constant and changing the basal uniform value of pumping $\bar{j}^a_0$ only. A uniform pumping profile leads to a typical distribution centered at the middle of the chain. To evaluate the effect of the perturbation with respect to the uniform pumping, we calculate the area below a region of width 2σ centered on the Gaussian and compare it with the area below the remaining quasi-uniform part of the profile of value $\sim \bar{j}^a_0$ (see Fig. 6B). This yields a typical threshold in basal pumping $\bar{j}^a_0 = \bar{j}^* \equiv \delta \bar{j}^a \frac{\sigma \sqrt{\pi}}{0.6 - 8\sigma} \mathrm{erf}(2)$ (see SI text). For a basal pumping rate $\bar{j}^a_0$ below the threshold $\bar{j}^* \simeq 0.44$, the perturbation dominates and the mean position of the final lumen is shifted to the maximum $x = \mu$ of the Gaussian. On the contrary, when the basal pumping rate $\bar{j}^a_0 > \bar{j}^*$, the two effects compete with each others, and the distribution for the final lumen localization may become bimodal (Fig. 6C). In spite of rapid diffusion within the intercellular space, the spatial localization of active pumping can therefore break the radial embryo symmetry by positioning the blastocoel away from the center of the network. In addition to mechanical differences between TE and ICM cells (8, 54), different rates of pumping between these two types of cells may constitute an alternative and fail-safe mechanism to ensure the robust localization of the blastocoel at the TE interface of mammalian embryos.

Discussion

We have presented a novel theory for the coarsening of a network of hydro-osmotically coupled biological cavities. From a physics perspective, coarsening processes have been the subject of a vast literature, with generally diffusion as the main mode of transport between dynamically coupled compartments (52). Only a few of them have considered hydrodynamic flows as an alternative mean for mass exchange (47, 49) and the influence of osmotic effects in coarsening have been studied mostly as a mean to stabilize emulsions or foams (45, 46). For a 1-dimensional chain, we find unexpectedly that our hydro-osmotic coarsening model exhibits, for a wide range of solvent and solute permeabilities, the same scaling dynamics $\mathcal{N} \sim t^{-2/5}$ as thin dewetting films, where an ensemble of droplets interacts through a thin fluid layer (48, 50, 51). This indicates that osmotic effects have generically a mild influence on the coarsening behavior in our model, that is ultimately dominated by hydraulic exchanges, as we hypothesized in (8). In contrast, we have showed that active ion pumping can largely affect collective lumen dynamics, with the emergence of a novel coarsening regime dominated by coalescence. The effect of active
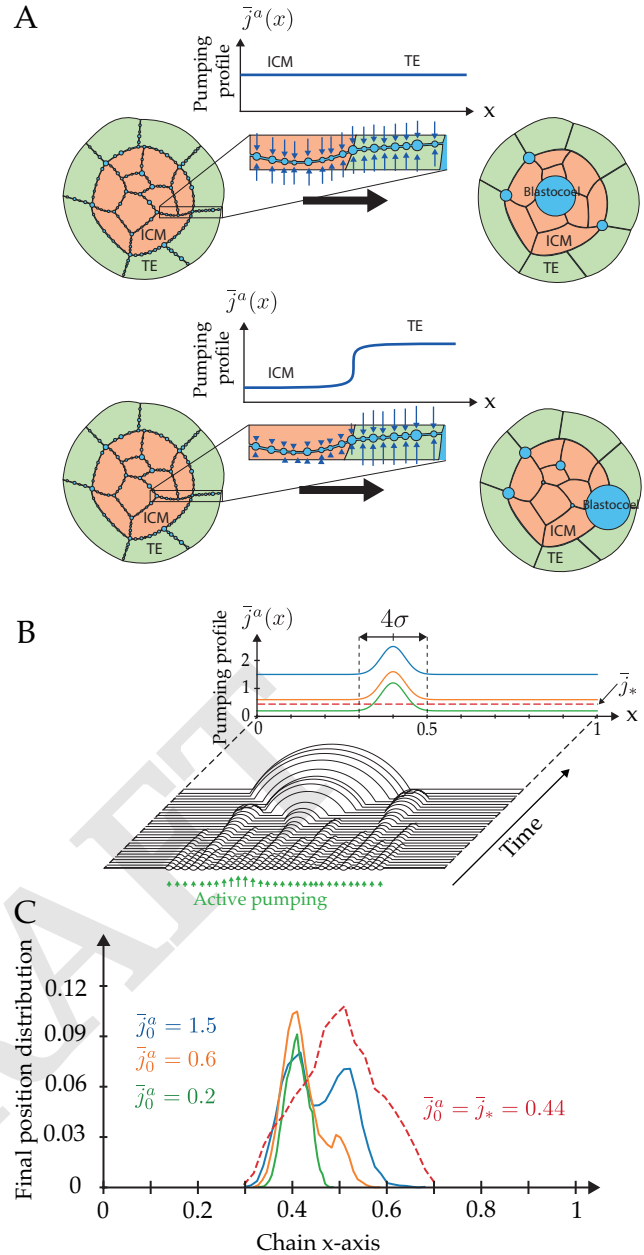

Fig. 6. (A) Schematic view of the embryo showing two cell-cell contact with heterogeneous active pumping. This heterogeneity leads to a symmetry breaking that positions the blastocoel at the Trophectoderm - Inner Cell Mass interface. (B) Plot of the pumping profiles along the chain and typical chain dynamics ($\mathcal{N}_0 = 30$). The uniform profile corresponds to the threshold $\bar{j}^* \simeq 0.44$ (dashed lines) and perturbed profiles are biased by a Gaussian in the form $\bar{j}^a(x) = \bar{j}^a_0 + \frac{\delta \bar{j}^a}{\sqrt{2\pi}\sigma} \exp\left(-\frac{(x-\mu)^2}{\sigma^2}\right)$ with basal pumping rates $\bar{j}^a_0 = 0.2, 0.6, 1.5$ and $\mu = 0.4$, $\sigma = 0.05$, $\delta \bar{j}^a = 1$. (C) Distributions for the localization of the final lumen on a chain of $\mathcal{N}_0 = 100$ lumens, corresponding to the pumping profiles depicted above. Each curve is obtained by averaging 10000 simulations with $\chi_v = 500$, $\chi_s = 1$.

pumping may be compared to droplet condensation on a surface (55, 56), but the absence of nucleation in our system constitutes a major difference that precludes a direct comparison of scaling behaviors (57, 58). The inclusion of lumen nucleation would require a precise microscopic description of the de-adhesion process, coupling membrane mechanics with stochastic binding-unbinding of adhesion molecules

(44). The addition of stochastic nucleation and short-time scale cortical and membrane dynamics to our model are undoubtedly interesting avenues to further refine the theory.

In spite of these simplifications our theory bring several generic, robust and experimentally testable predictions. In particular, we expect our theory to be relevant, beyond lumenogenesis, to describe the hydraulic cell coarsening phenomena underlying *Drosophila* and *C. elegans* oogenesis (35, 37, 38). Our theory demonstrates that lumen coarsening exhibits a generic dynamic scaling behavior. Extrapolating this behavior to the realistic topology of microlumens in 3D, that form a continuous 2D network at each cell-cell interface, one would predict a scaling law $\mathcal{N} \sim t^{-3/4}$ for the number of lumens (59). Whether the slighlty more complex topology of the embryo, where cell arrangements form themselves a 3D network of cell-cell contacts, might affect the late scaling dynamics remains however to be tested. This scaling behavior relies essentially on the hydraulic coupling between lumens. Interestingly, if one compares the typical diameter of an embryo or small tissue ($50 - 100\mu m$) with a typical pressure screening length $\xi_v \sim 84\mu m$ (see Table S1), the microlumens are expected to remain hydraulically coupled during the whole coarsening process, ensuring hence the robust formation of a single cavity. To test and challenge this aspect, it could be interesting to artificially merge two or more embryos before blastulation to see if several, uncoupled, cavities may form. One major simplification in our theory is to neglect the local mechanical response of surrounding cells to lumens deformations. As cell mechanics enters essentially in the small parameter $\epsilon = \frac{\gamma \sin \theta}{L_0 \Pi_0}$ in our model, we do not expect cell mechanics to fundamentally affect the scaling behavior. We hence verify that the scaling exponent remains unaffected by ϵ, as long as it remains smaller than 10^{-1} (see Fig. S3), which is lower than a typical upper estimation 10^{-2} for embryos. As we have shown in (8), gradients of cell mechanical properties can however be sufficient to spatially bias the coarsening. Interestingly, a similar control of coarsening by stiffness gradients was also recently demonstrated in the context of Ostwald ripening (60, 61). A second major assumption of our theory is to consider only one and non-charged solute, while cell volume control is known to rely on a pump-leak mechanism that involves, at minimum, three major ionic species K^+, Na^+ and Cl^- (62). Our choice was first motivated by the sake of simplicity but turned out to largely ease the numerical treatment of the equations. Indeed, each ion taken individually has a large concentration differences between cytoplasmic and external compartments (K^+ is essentially cytoplasmic while Na^+ and Cl^- are concentrated in the external medium), which would prevent us to asymptotically expand logarithms in chemical potentials. In contrast, the global osmolarity difference remains small compared to its typical absolute value $\delta c \gg c_0$, which allowed us to find analytic solutions in bridges, and to reformulate the dynamics as a simple system of coupled ordinary equations to perform extensive numerical simulations. The addition of charged species would furthermore require to consider explicitly membrane potentials and electrodiffu-

sion effects, opening novel questions such as the existence of electrical currents and elecro-osmotic flows between lumens. These questions are beyond the scope of this manuscript and will require ample effort in terms of theoretical modeling and numerical work. They undoubtedly open exciting novel avenues of research on the still largely overlooked roles of bioelectricity in development and tissue morphogenesis (63, 64).

Materials and Methods

Coupled differential equations are solved numerically using a Runge-Kutta-Fehlberg method (RKF45) with adaptative time-step (65, 66). Topological transitions such as coalescence of two lumens or deletion of an empty lumen are automatically detected and handled by our numerical scheme (see Fig. S4 and SI text for details). On Fig. 3, the classification of events is determined by the sign of the final slopes for the time evolution of lumen area (see SI for details).

The simulation code and Python notebooks for analysis of the results are available on the following repository: https://github.com/VirtualEmbryo/hydroosmotic_chain

Bibliography

1. Lewis Wolpert, Cheryll Tickle, and Alfonso Martinez Arias. *Principles of development*. Oxford University Press, USA, 2015.
2. L Wolpert and T Gustafson. Studies on the cellular basis of morphogenesis of the sea urchin embryo. *Experimental Cell Research*, 25(2):374–382, November 1961.
3. M Dan-Sohkawa and H Fujisawa. Cell dynamics of the blastulation process in the starfish, Asterina pectinifera. *Developmental Biology*, 77(2):328–339, June 1980.
4. D Drasdo and G Forgacs. Modeling the interplay of generic and genetic mechanisms in cleavage, blastulation, and gastrulation. *Developmental dynamics : an official publication of the American Association of Anatomists*, 219(2):182–191, October 2000.
5. Lawrence Bodenstein. Simulations of sea urchin early development delineate the role of oriented cell division in the morula-to-blastula transition. *MOD*, 162:103606, June 2020.
6. Tom P Fleming, Tom Papenbrock, Irina Fesenko, Peter Hausen, and Bhavwanti Sheth. Assembly of tight junctions during early vertebrate development. *Seminars in Cell & Developmental Biology*, 11(4):291–299, August 2000.
7. C S Merzdorf, Y H Chen, and D A Goodenough. Formation of functional tight junctions in Xenopus embryos. *Developmental Biology*, 195(2):187–203, March 1998.
8. Julien G. Dumortier, Mathieu Le Verge-Serandour, Anna Francesca Tortorelli, Annette Mielke, Ludmilla de Plater, Hervé Turlier, and Jean-Léon Maître. Hydraulic fracturing and active coarsening position the lumen of the mouse blastocyst. *Science*, 365(6452):465–468, aug 2019. ISSN 0036-8075. doi: 10.1126/science.aaw7709.
9. Katsuyuki Miyaguchi. Ultrastructure of the Zonula Adherens Revealed by Rapid-Freeze Deep-Etching. *Journal of Structural Biology*, 132(3):169–178, December 2000.
10. Susanne F. Fenz, Rudolf Merkel, and Kheya Sengupta. Diffusion and Intermembrane Distance: Case Study of Avidin and E-Cadherin Mediated Adhesion. *Langmuir*, 25(2):1074–1085, jan 2009. ISSN 0743-7463. doi: 10.1021/la803227s.
11. J. E. Fléchon, M. Panigel, D. C. Kraemer, S. S. Kalter, and E. S.E. Hafez. Surface ultrastructure of preimplantation baboon embryos. *Anatomy and Embryology*, 149(3):289–295, 1976. ISSN 03402061. doi: 10.1007/BF00315444.
12. P R Hurst, K Jefferies, P Eckstein, and A G Wheeler. An ultrastructural study of preimplantation uterine embryos of the rhesus monkey. *Journal of anatomy*, 126(Pt 1):209–20, 1978. ISSN 0021-8782.
13. P H TUFT. The uptake and distribution of water in the embryo of Xenopus laevis (Daudin). *Journal of Experimental Biology*, 39:1–19, March 1962.
14. M. R. Kalt. The relationship between cleavage and blastocoel formation in Xenopus laevis. II. Electron microscopic observations. *Journal of Embryology and Experimental Morphology*, 26(1):51–66, 1971. ISSN 00220752.
15. Debanjan Barua, Serge E. Parent, and Rudolf Winklbauer. Mechanics of Fluid-Filled Interstitial Gaps. II. Gap Characteristics in Xenopus Embryonic Ectoderm. *Biophysical Journal*, 113(4):923–936, 2017. ISSN 15420086. doi: 10.1016/j.bpj.2017.06.063.
16. Jeremy Nance and James R. Priess. Cell polarity and gastrulation in C. elegans. *Development (Cambridge, England)*, 129(2):387–97, jan 2002. ISSN 0950-1991.
17. R M Borland, J D Biggers, and C P Lechene. Studies on the composition and formation of mouse blastocoele fluid using electron probe microanalysis. *Developmental Biology*, 55(1):1–8, January 1977.

18. L M Wiley. Cavitation in the mouse preimplantation embryo: Na/K-ATPase and the origin of nascent blastocoele fluid. *Developmental Biology*, 105(2):330–342, October 1984.

19. Peter Mazur and Ulrich Schneider. Osmotic responses of preimplantation mouse and bovine embryos and their cryobiological implications. *Cell Biophysics*, 8(4):259–285, aug 1986. ISSN 0163-4992. doi: 10.1007/BF02788516.

20. Lisa C Barcroft, Hanne Offenberg, Preben Thomsen, and Andrew J Watson. Aquaporin proteins in murine trophectoderm mediate transepithelial water movements during cavitation. *Developmental Biology*, 256(2):342–354, April 2003.

21. Rikako Kawagishi, Masahiro Tahara, Kenjiro Sawada, Kenichiro Morishige, Masahiro Sakata, Keiichi Tasaka, and Yuji Murata. Na+/H+ Exchanger-3 is involved in mouse blastocyst formation. *Journal of Experimental Zoology*, 301A(9):767–775, 2004.

22. Katsuma Dan. Cyto-embryological studies of sea urchins. II. Blastula stage. *The Biological Bulletin*, 102(1):74–89, February 1952.

23. Søren Løvtrup. Water permeation in the amphibian embryo. *Journal of Experimental Zoology*, 145(2):139–149, November 1960.

24. LC Beadle. Salt and Water Regulation in the Embryos of Freshwater Pulmonate Molluscs: III. Regulation of Water During the Development of Biomphalaria Sudanica. *Journal of Experimental Biology*, 20(2):491–499, 1969.

25. M Cereijido, E S Robbins, W J Dolan, C A Rotunno, and D D Sabatini. Polarized monolayers formed by epithelial cells on a permeable and translucent support. *Journal of Cell Biology*, 77(3):853–880, June 1978.

26. J E Lever. Inducers of mammalian cell differentiation stimulate dome formation in a differentiated kidney epithelial cell line (MDCK). *PNAS*, 76(3):1323–1327, March 1979.

27. A Z Wang, G K Ojakian, and W J Nelson. Steps in the morphogenesis of a polarized epithelium. I. Uncoupling the roles of cell-cell and cell-substratum contact in establishing plasma membrane polarity in multicellular epithelial (MDCK) cysts. *Journal of Cell Science*, 95 (Pt 1):137–151, January 1990.

28. A Z Wang, J C Wang, G K Ojakian, and W J Nelson. Determinants of apical membrane formation and distribution in multicellular epithelial MDCK cysts. *The American journal of physiology*, 267(2 Pt 1):C473–81, August 1994.

29. Sara Sigurbjörnsdóttir, Renjith Mathew, and Maria Leptin. Molecular mechanisms of de novo lumen formation. *Nature Reviews Molecular Cell Biology*, 15(10):665–676, oct 2014. ISSN 1471-0072. doi: 10.1038/nrm3871.

30. Yue Zhang, Richard De Mets, Cornelia Monzel, Vidhyalakshmi Acharya, Pearlyn Toh, Jasmine Fei Li Chin, Noamp x000E9 mi Van Hul, Inn Chuan Ng, Hanry Yu, Soon Seng Ng, S Tamir Rashid, and Virgile Viasnoff. Biomimetic niches reveal the minimal cues to trigger apical lumen formation in single hepatocytes. *Nature Materials*, pages 1–15, April 2020.

31. Susanne M Krug, Jörg D Schulzke, and Michael Fromm. Tight junction, selective permeability, and related diseases. *Seminars in Cell & Developmental Biology*, 36:166–176, December 2014.

32. Vani Narayanan, Laurel E Schappell, Carl R Mayer, Ashley A Duke, Travis J Armiger, Paul T Arsenovic, Abhinav Mohan, Kris N Dahl, Jason P Gleghorn, and Daniel E Conway. Osmotic Gradients in Epithelial Acini Increase Mechanical Tension across E-cadherin, Drive Morphogenesis, and Maintain Homeostasis. *Current Biology*, 30(4):624–633.e4, February 2020.

33. J M Torkko, A Manninen, S Schuck, and K Simons. Depletion of apical transport proteins perturbs epithelial cyst formation and ciliogenesis. *Journal of Cell Science*, 121(8):1193–1203, April 2008.

34. Sabyasachi Dasgupta, Kapish Gupta, Yue Zhang, Virgile Viasnoff, and Jacques Prost. Physics of lumen growth. *Proceedings of the National Academy of Sciences*, 115(21): E4751–E4757, may 2018. doi: 10.1073/pnas.1722154115.

35. Laurie-Anne Lamiré, Pascale Milani, Gaël Runel, Annamaria Kiss, Leticia Arias, Blandine Vergier, Pradeep Das, David Cluet, Arezki Boudaoud, and Muriel Grammont. A gradient in inner pressure of germline cells controls overlaying epithelial cell morphogenesis. *BioRxiv*, page 440438, 2018.

36. Chii Jou Chan, Maria Costanzo, Teresa Ruiz-Herrero, Gregor Mamp x000F6 nke, Ryan J Petrie, Martin Bergert, Alba Diz-Muamp x000F1 oz, L Mahadevan, and Takashi Hiiragi. Hydraulic control of mammalian embryo size and cell fate. *Nature*, pages 1–22, June 2019.

37. Jasmin Imran Alsous, Nicolas Romeo, Jonathan A Jackson, Frank Mason, Jörn Dunkel, and Adam C Martin. Dynamics of hydraulic and contractile wave-mediated fluid transport during Drosophila oogenesis. *BioRxiv*, 38:15109–50, September 2020.

38. Nicolas T Chartier, Arghyadip Mukherjee, Julia Pfanzelter, Sebastian Früthauer, Ben T Larson, Anatol W Fritsch, Moritz Kreysing, Frank Jülicher, and Stephan W Grill. A hydraulic instability drives the cell death decision in the nematode germline. pages 1–16, May 2020.

39. Karen Alim. Fluid flows shaping organism morphology. *Philosophical Transactions of the Royal Society B: Biological Sciences*, 373(1747):20170112–5, April 2018.

40. Ibrahim Cheddadi, Michel Génard, Nadia Bertin, and Christophe Godin. Coupling water fluxes with cell wall mechanics in a multicellular model of plant development. *PLoS computational biology*, 15(6):e1007121–16, June 2019.

41. Monika Dolega, Giuseppe Zurlo, Magali Le Goff, Magdalena Greda, Claude Verdier, J-F Joanny, Giovanni Cappello, and Pierre Recho. Mechanical behavior of multi-cellular spheroids under osmotic compression. *Journal of the Mechanics and Physics of Solids*, page 104205, 2020.

42. Yuchen Long, Ibrahim Cheddadi, Gabriella Mosca, Vincent Mirabet, Mathilde Dumond, Annamaria Kiss, Jan Traas, Christophe Godin, and Arezki Boudaoud. Cellular Heterogeneity in Pressure and Growth Emerges from Tissue Topology and Geometry. *Current Biology*, 30 (8):1504–1516.e8, April 2020.

43. Marino Arroyo and Xavier Trepat. Hydraulic fracturing in cells and tissues: fracking meets cell biology. *Current Opinion in Cell Biology*, 44:1–6, feb 2017. ISSN 09550674. doi: 10.1016/j.ceb.2016.11.001.

44. Dimitri Kaurin and Marino Arroyo. Surface Tension Controls the Hydraulic Fracture of Adhesive Interfaces Bridged by Molecular Bonds. *Physical Review Letters*, 123(22):228102, nov 2019. ISSN 0031-9007. doi: 10.1103/PhysRevLett.123.228102.

45. A. J. Webster and M. E. Cates. Stabilization of emulsions by trapped species. *Langmuir*, 14 (8):2068–2077, 1998. ISSN 07437463. doi: 10.1021/la9712597.

46. A. J. Webster and M. E. Cates. Osmotic Stabilisation of Concentrated Emulsions and Foams. *Langmuir*, 17(18):595–608, 2001. doi: 10.1021/la000699m.

47. Len M. Pismen and Yves Pomeau. Mobility and interactions of weakly nonwetting droplets. *Physics of Fluids*, 16(7):2604–2612, jul 2004. ISSN 1070-6631. doi: 10.1063/1.1758911.

48. K.B. Glasner and T.P. Witelski. Collision versus collapse of droplets in coarsening of dewetting thin films. *Physica D: Nonlinear Phenomena*, 209(1-4):80–104, sep 2005. ISSN 01672789. doi: 10.1016/j.physd.2005.06.010.

49. Henrik B. van Lengerich, Michael J. Vogel, and Paul H. Steen. Coarsening of capillary drops coupled by conduit networks. *Physical Review E*, 82(6):066312, dec 2010. ISSN 1539-3755. doi: 10.1103/PhysRevE.82.066312.

50. K. B. Glasner and Thomas P. Witelski. Coarsening dynamics of dewetting films. *Physical Review E - Statistical Physics, Plasmas, Fluids, and Related Interdisciplinary Topics*, 67(1): 12, 2003. ISSN 1063651X. doi: 10.1103/PhysRevE.67.016302.

51. Michael B. Gratton and Thomas P. Witelski. Transient and self-similar dynamics in thin film coarsening. *Physica D: Nonlinear Phenomena*, 238(23-24):2380–2394, dec 2009. ISSN 01672789. doi: 10.1016/j.physd.2009.09.015.

52. I.M. Lifshitz and V.V. Slyozov. The kinetics of precipitation from supersaturated solid solutions. *Journal of Physics and Chemistry of Solids*, 19(1-2):35–50, apr 1961. ISSN 00223697. doi: 10.1016/0022-3697(61)90054-3.

53. J D Biggers, J E Bell, and D J Benos. Mammalian blastocyst: transport functions in a developing epithelium. *The American journal of physiology*, 255(4 Pt 1):C419–32, October 1988.

54. Jean-léon Maître, Hervé Turlier, Rukshala Illukkumbura, Björn Eismann, Ritsuya Niwayama, François Nédélec, and Takashi Hiiragi. Asymmetric division of contractile domains couples cell positioning and fate specification. *Nature*, 536(7616):344–348, August 2016.

55. Jean Louis Viovy, Daniel Beysens, and Charles M Knobler. Scaling description for the growth of condensation patterns on surfaces. *Physical Review A*, 37(12):4965–4970, jun 1988. ISSN 0556-2791. doi: 10.1103/PhysRevA.37.4965.

56. T. M. Rogers, K. R. Elder, and Rashmi C. Desai. Droplet growth and coarsening during heterogeneous vapor condensation. *Physical Review A*, 38(10):5303–5309, nov 1988. ISSN 0556-2791. doi: 10.1103/PhysRevA.38.5303.

57. B. Derrida, C. Godrèche, and I. Yekutieli. Scale-invariant regimes in one-dimensional models of growing and coalescing droplets. *Physical Review A*, 44(10):6241–6251, nov 1991. ISSN 1050-2947. doi: 10.1103/PhysRevA.44.6241.

58. L. Stricker and J. Vollmer. Impact of microphysics on the growth of one-dimensional breath figures. *Physical Review E*, 92(4):042406, oct 2015. ISSN 1539-3755. doi: 10.1103/PhysRevE.92.042406.

59. Henrik B. van Lengerich, Michael J. Vogel, and Paul H. Steen. Coarsening of capillary drops coupled by conduit networks. *Physical Review E*, 82(6):066312, dec 2010. ISSN 1539-3755. doi: 10.1103/PhysRevE.82.066312.

60. Kathryn A Rosowski, Estefania Vidal-Henriquez, David Zwicker, Robert W Style, and Eric R Dufresne. Elastic stresses reverse Ostwald ripening. *Soft Matter*, 16(25):5892–5897, 2020.

61. Estefania Vidal-Henriquez and David Zwicker. Theory of droplet ripening in stiffness gradients. *Soft Matter*, 16(25):5898–5905, 2020.

62. Yoichiro Mori. Mathematical properties of pump-leak models of cell volume control and electrolyte balance. *Journal of Mathematical Biology*, 65(5):875–918, November 2011.

63. Michael Levin. Molecular bioelectricity in developmental biology: New tools and recent discoveries. *BioEssays*, 34(3):205–217, January 2012.

64. Charlie Duclut, Niladri Sarkar, Jacques Prost, and Frank Jülicher. Fluid pumping and active flexoelectricity can promote lumen nucleation in cell assemblies. *PNAS*, 116(39):19264–19273, September 2019.

65. Erwin Fehlberg. Low-Order Classical Runge-Kutta Formulas with Stepsize Control and their Application to Some Heat Transfer Problems. *NASA Technical Reports*, 315, 1969.

66. William H. Press and Saul A. Teukolsky. Adaptive Stepsize Runge-Kutta Integration. *Computers in Physics*, 6(2):188, 1992. ISSN 08941866. doi: 10.1063/1.4823060.